Research Article Vol. 14, No. 3 / 1 Mar 2023 / Biomedical Optics Express 1256
Biomedical Optics EXPRESS

# Dysplasia and tumor discrimination in brain tissues by combined fluorescence, Raman, and diffuse reflectance spectroscopies

ENRICO BARIA,[1,2] FLAVIO GIORDANO,[3] RENZO GUERRINI,[3] CHIARA CAPORALINI,[4] ANNA MARIA BUCCOLIERO,[4] RICCARDO CICCHI,[1,2,*] AND FRANCESCO SAVERIO PAVONE[1,2,5]

[1]*National Institute of Optics, National Research Council, Via Nello Carrara 1, Sesto Fiorentino 50019, Italy*
[2]*European Laboratory for Non-Linear Spectroscopy, University of Florence, Via Nello Carrara 1, Sesto Fiorentino 50019, Italy*
[3]*Division of Neurosurgery, Department of Neuroscience I, Meyer Children's Hospital IRCCS, Viale Gaetano Pieraccini 24, Florence 50141, Italy*
[4]*Division of Pathology, Department of Critical Care Medicine and Surgery, University of Florence, Viale Giovanni Battista Morgagni 85, Florence 50134, Italy*
[5]*Department of Physics and Astrophysics, University of Florence, Via Sansone 1, Sesto Fiorentino 50019, Italy*
[*]*riccardo.cicchi@ino.cnr.it*

**Abstract:** Identification of neoplastic and dysplastic brain tissues is of paramount importance for improving the outcomes of neurosurgical procedures. This study explores the combined application of fluorescence, Raman and diffuse reflectance spectroscopies for the detection and classification of brain tumor and cortical dysplasia with a label-free modality. Multivariate analysis was performed to evaluate classification accuracies of these techniques–employed both in individual and multimodal configuration–obtaining high sensitivity and specificity. In particular, the proposed multimodal approach allowed discriminating tumor/dysplastic tissues against control tissue with 91%/86% sensitivity and 100%/100% specificity, respectively, whereas tumor from dysplastic tissues were discriminated with 89% sensitivity and 86% specificity. Hence, multimodal optical spectroscopy allows reliably differentiating these pathologies using a non-invasive, label-free approach that is faster than the gold standard technique and does not require any tissue processing, offering the potential for the clinical translation of the technology.



## 1. Introduction

Neurosurgery is the first choice treatment of brain focal cortical dysplasia (FCD) leading to drug-resistant epilepsy [1], and both low and high grade gliomas [2]. The aim of surgery is achieving a radical resection without damaging the healthy brain tissue, especially in case of infiltrating high-grade gliomas, the boundaries of which are not always clearly detectable by visual inspection. Besides pure neuro-oncological issues when dealing with gliomas, radical resection of FCDs is associated with the best control of seizures. Neuronavigation may provide useful information, but is limited by brain shifts [3], occurring during surgery after craniotomy, since it relies upon static pre-operative MRIs. Real time intraoperative imaging techniques – typically based on ultrasounds (iUS) and magnetic resonance (iMRI) – have been proposed to cope with this limits with interesting applications [4]. On the other side, they carry important drawbacks [5]: iUS is cheap but cannot provide functional information, and its accuracy can be affected by artifacts and low image quality; iMRI offers real-time feedback and high resolution but has very high costs, requires a dedicated operating room equipped with antimagnetic tools, and to stop surgery in order to get MRI images. Moreover, FCD and tumor borders are often blurred and cannot be always defined with precision by current techniques especially in case of

#477035 https://doi.org/10.1364/BOE.477035
Journal © 2023 Received 7 Oct 2022; revised 19 Dec 2022; accepted 19 Dec 2022; published 24 Feb 2023

Biomedical Optics EXPRESS

diffuse cortical malformation and gliomas [6,7]. Another critical point is the frequent association between low grade gliomas (the so-called Long-term Epilepsy Associated Tumors – LEATs) with FCD, corresponding to FCD type IIIb, according to ILAE 2011 Classification [8]. Clinical manifestations and standard imaging findings of these two pathologies may be similar [9], preventing a timely recognition of neoplastic contents. A possible solution to these issues is provided by standard histopathological, intraoperative analysis of resected biopsies to provide a preliminary diagnosis; this is, however, a labor- and time-consuming process that significantly lengthens the surgery. Hence, there are currently unmet needs for clinical diagnosis and *in situ* demarcation of both brain tumor and FCD.

In this context, different optical methods have been developed and applied for brain tissue diagnostics and, particularly, tumor detection. Among them, fluorescence (with [10] or without [11] preoperatively administered contrast agents), Raman [12,13] and diffuse reflectance [14,15] are well-known spectroscopic techniques, each offering unique sensitivity to specific biochemical features of the examined tissues. In fact, endogenous fluorescence can be used to highlight intrinsic biomarkers involved in metabolism, such as nicotinamide adenine dinucleotide (NADH) and flavin adenine dinucleotide (FAD). Raman spectra allow analyzing tissue molecular composition based on the specific vibration modes of body molecules, allowing to identify and quantify – for example – proteins and lipids. Diffuse reflectance investigates absorption/reflection properties of tissues and their intrinsic chromophores, e.g. water and hemoglobin content in human organs. The advantage of retrieving multiple types of information in a fast and label-free approach has favored multimodal solutions combining two or more optical methods [16–18]. Moreover, increased application of machine learning algorithms for biological classification based on spectroscopic data [19,20] is paving the way for automated, operator-independent diagnosis of brain pathologies, both *in vivo* and *ex vivo*.

A sizable literature on the use of optical spectroscopy is already available for brain tumor detection, while, to the best of our knowledge, only one study addressed FCD [18]. Therefore, we used Raman, fluorescence and diffuse reflectance fiber-probe spectroscopies – organized in a label-free and multimodal configuration – for examining fresh brain biopsies affected by either neoplastic or dysplastic pathologies. We also developed spectral classifiers for discriminating these diseases from control brain tissue and for differentiating the two pathologies. These findings suggest that a diagnostic approach based on multimodal spectroscopy could provide an additional tool to detect with higher precision the boundaries of FCDs and gliomas in order to get a radical resection for neuro-oncological purposes and to achieve the best control of epilepsy.

## 2. Materials and methods

A multimodal optical device based on UV/visible-excited fluorescence, NIR-excited Raman and diffuse reflectance spectroscopies was employed for examining freshly excised brain tissues.

### 2.1. Samples

This study was approved by the Medical Ethics Review Board of the Anna Meyer Children's Hospital (M-AZI015-00, 21/04/2021) in Florence, Italy, and conducted according to the tenets of the Declaration of Helsinki. 51 pediatric patients (0÷18 years old) suffering from either neoplastic (21 cases), dysplastic (25 cases) or other diseases (e.g. gliosis / reactive alterations; 5 cases) underwent brain surgery, and were included in the study after obtaining informed consent from all participants and guardians.

Freshly excised tissue specimens of pathological brain tissue were put in saline solution and immediately transported to the laboratory for spectroscopic measurements. In a few occasions, cortex and subcortical white matter of deeper brain structures were collected when the surgical procedure required it.

Biomedical Optics EXPRESS

### 2.2. Experimental setup

The experimental setup used in this study was previously described in [16,21] and consists of four excitation sources, a custom-made fiber-probe, and a detection system (Fig. 1).

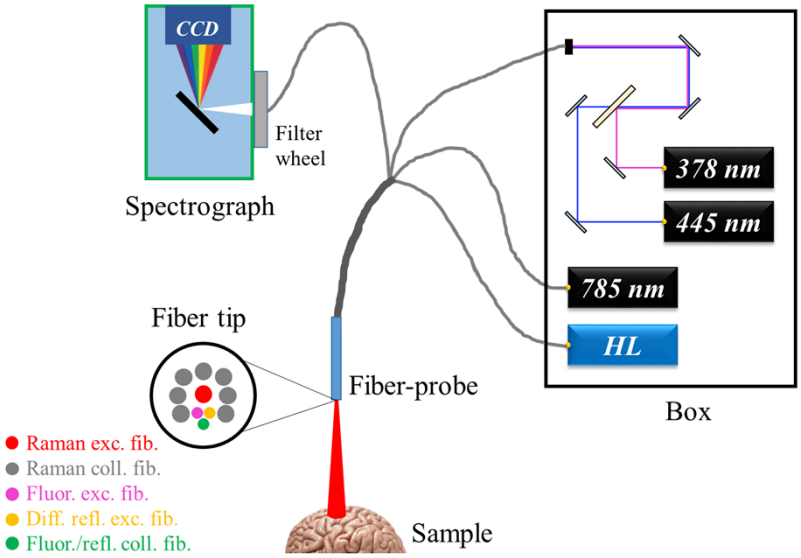


**Fig. 1.** Drawing of the experimental setup: a box $45 \times 30 \times 25$ cm$^3$ in size contains 3 CW lasers and a halogen lamp, which are connected to the Raman, fluorescence and diffuse reflectance excitation fibers of a quadrifurcated fiber-probe. The collection fibers at the tip of the probe collect Raman, fluorescence and diffuse reflectance signals, delivering them to a detection system based on a spectrograph and a CCD camera.

Two CW lasers (TEC 042, Sacher Lasertechnik, Marburg, Germany) emitting at 378 nm and 445 nm are used to perform, respectively, UV- and visible-excited fluorescence spectroscopy. An additional CW laser at 785 nm (FC-785-350-MM2-PC-1-0-RM, RGBLase, Fremont, California) is employed for generating Raman signals in the NIR region of the spectrum. A halogen lamp (HL-2000-LL, Ocean Optics, Dunedin, Florida) provides broadband excitation light for reflectance measurements.

These sources are connected to a quadri-furcated, custom-made fiber-probe (EMVision LCC, Loxahatchee, Florida) consisting of 11 optical fibers: a central fiber (300 µm core diameter) for delivering 785 nm laser light; 7 surrounding fibers (300 µm each) for Raman collection; 2 fibers (200 µm each) for delivering 378/445 nm and white-light from the halogen lamp, respectively, and 1 fiber (200 µm) for collecting both fluorescence and diffuse reflectance signals, all of them placed near to the central fiber. A narrow bandpass filter centered at 785 nm is placed in front of the Raman delivering fiber to clean the laser line, blocking unwanted fluorescence and Raman signals generated inside the optical fiber itself. A ring-shaped long-pass optical filter is placed at the distal end of the probe, preventing 785-nm laser light from entering the seven Raman collection fibers.

These collection fibers are aligned inside a ferrule and connected to a spectrograph (MicroHR, HORIBA Scientific, Edison, New Jersey) equipped with a 600 lines/mm grating and with an open-electrode CCD camera (Syncerity, HORIBA Scientific, Edison, New Jersey) cooled at −60°C. A motorized filter wheel – placed at the entrance of the spectrograph – allows changing emission filter according to the spectral technique used: a long pass filter at 400 nm (Longpass 400 nm, Melles Griot, Albuquerque, New Mexico) for fluorescence spectroscopy excited at 378 nm; a

Biomedical Optics EXPRESS

long pass filter at 458 nm (LP02-458RS-25, Semrock, Rochester, New York) for fluorescence spectroscopy excited at 445 nm; a long pass filter at 785 nm (LP02-785RE-25, Semrock) for Raman spectroscopy; and a neutral density filter with OD = 0.3 for diffuse reflectance. These filters prevent laser light from entering the spectrograph and lamp light from saturating the detector.

The setup has been compacted to make it transportable on a medical trolley. The last 10 cm of the fiber-probe are protected by a metal jacket, allowing it to be easily handled (as a pen) for *in vivo* examination of suspicious tissue areas. However, since this experiment was conducted *ex vivo*, the probe was kept steady upon each sample by a custom-made holder.

### 2.3. Measurement protocol

Prior to each session of measurements, a spectral calibration of the spectrograph was performed by using emission lines from a Neon-Argon lamp as references. Then, collected biopsies (usually 1÷3 cm in size) were placed upon a microscope slide covered with black tape to avoid any spectral contribution from the sample holder. The fiber-probe was put in gentle contact with the tissue at 2÷5 locations per biopsy, the number of examined sites depending on its size. A single acquisition typically required 0.01÷0.5 s for fluorescence, 1÷5 s for Raman and 0.001÷0.05 s for diffuse reflectance; 10 acquisitions were recorded and averaged from each site to improve the signal-to-noise ratio. The optical inspection required less than 2 minutes for each site, and the distal end of the probe was cleaned with ethanol solution thereafter. In total, 163 sites were examined: 94 from dysplastic tissues, 54 from tumor tissues, and 15 from non-dysplastic and non-neoplastic ("control") brain tissues. All fluorescence, Raman and diffuse reflectance spectra were co-registered from the same tissue volumes and recorded within 30 minutes from surgical resection. Finally, each biopsy was put in formalin solution and submitted to pathologists for common routine histology; the histopathology results for all patients included in the study are reported in Table 1.

### 2.4. Data analysis

Fluorescence, Raman and diffuse reflectance spectra were pre-processed before being analyzed by two alternative classification methods. The following paragraphs thoroughly describe these steps, and Fig. 2 shows a schematic representation of the analysis.

#### 2.4.1. Spectral pre-processing

The emission spectrum of a radiometrically calibrated halogen lamp (HL-3P-CAL, Ocean Optics, Dunedin, Florida) was recorded by illuminating a reflectance standard (WS1, Ocean Optics, Dunedin, Florida) for all the spectral ranges and optical filters used during fluorescence and Raman measurements. The transmission spectrum of the fiber-probe setup was obtained by calculating the ratio between the "real" emission spectrum (provided by the vendor of the calibrated light source) and the recorded spectrum. Then, the transmission spectrum was used for correcting all recorded fluorescence and Raman spectra to remove spectral artifacts generated by the setup. In addition, 5-points boxcar smoothing and a $5^{th}$-order polynomial fitting was implemented through an automated routine, Vancouver Raman algorithm (VRA [22]), for removing NIR fluorescence and background signals from the Raman spectra. Finally, fluorescence and Raman spectra were normalized according to their maximum and total intensity, respectively. Diffuse reflectance spectra were corrected for lamp emission spectrum and normalized to the intensity recorded at 570 nm, which is one of the oxy/deoxy-hemoglobin isosbestic points.

The normalized dataset of each technique – fluorescence excited at 378 nm ("Fluo-378"), fluorescence excited at 445 nm ("Fluo-445"), Raman, diffuse reflectance – was analyzed through Principal Component Analysis (PCA), a well-known methodology [23] for reducing noise and redundant information. The first 15 principal components (PCs) were initially selected; we later

Biomedical Optics EXPRESS

**Table 1. Summary of patients' histopathology reports[a]**

| | Histopathological report | Assigned class |
|---|---|---|
| 1 | Reactive gliosis | Control |
| 2 | Perilesional tissue (from a case of reactive gliosis) | Control |
| 3 | Perilesional tissue (from a case of meningioangiomatosis) | Control |
| 4 | Astrogliosis, microglial activation | Control |
| 5 | Reactive gliosis | Control |
| 6 | FCD IIB | Dysplasia |
| 7 | FCD Ic | Dysplasia |
| 8 | FCD IIA | Dysplasia |
| 9 | FCD IIA | Dysplasia |
| 10 | Dysplastic lesion | Dysplasia |
| 11 | FCD IIb | Dysplasia |
| 12 | Disrupted cortical lamination, without balloon cells and dysmorphic neurons | Dysplasia |
| 13 | Hemimegalencephaly | Dysplasia |
| 14 | FCD Ib | Dysplasia |
| 15 | FCD IIb | Dysplasia |
| 16 | Disrupted cortical lamination in presence of reactive gliosis | Dysplasia |
| 17 | Disrupted cortical lamination | Dysplasia |
| 18 | Disrupted cortical lamination | Dysplasia |
| 19 | Disrupted cortical lamination | Dysplasia |
| 20 | FCD IIb | Dysplasia |
| 21 | FCD Ib | Dysplasia |
| 22 | FCD Ib | Dysplasia |
| 23 | Disrupted cortical lamination with dysmorphic neurons | Dysplasia |
| 24 | FCD IIB | Dysplasia |
| 25 | FCD IIIA | Dysplasia |
| 26 | Disrupted cortical lamination with dysmorphic neurons | Dysplasia |
| 27 | Malformation of cortical development | Dysplasia |
| 28 | Disrupted cortical lamination | Dysplasia |
| 29 | Disrupted cortical lamination | Dysplasia |
| 30 | Disrupted cortical lamination | Dysplasia |
| 31 | LGG | Tumor |
| 32 | Glioneuronal LGG | Tumor |
| 33 | Ganglioma | Tumor |
| 34 | Low-grade glioneuronal tumor | Tumor |
| 35 | Ependymoma II | Tumor |
| 36 | LGA | Tumor |
| 37 | Pilocytic astrocytoma | Tumor |
| 38 | LGA | Tumor |
| 39 | High-grade glioma | Tumor |
| 40 | Glial neoplasm | Tumor |
| 41 | LGG | Tumor |
| 42 | Astrocytoma | Tumor |
| 43 | Low-grade glioneuronal tumor | Tumor |
| 44 | Pilocytic astrocytoma | Tumor |
| 45 | Gangliоglioma | Tumor |
| 46 | Low-grade glioneuronal neoplasm | Tumor |
| 47 | Low-grade glioneuronal neoplasm | Tumor |
| 48 | LGA | Tumor |
| 49 | Glioneuronal tumor | Tumor |
| 50 | Gangliоglioma | Tumor |
| 51 | Low-grade glioneuronal tumor | Tumor |

[a]Acronyms: LGG = low-grade ganglioma; FCD = focal cortical dysplasia; LGA = low-grade astrocytoma.

Biomedical Optics EXPRESS

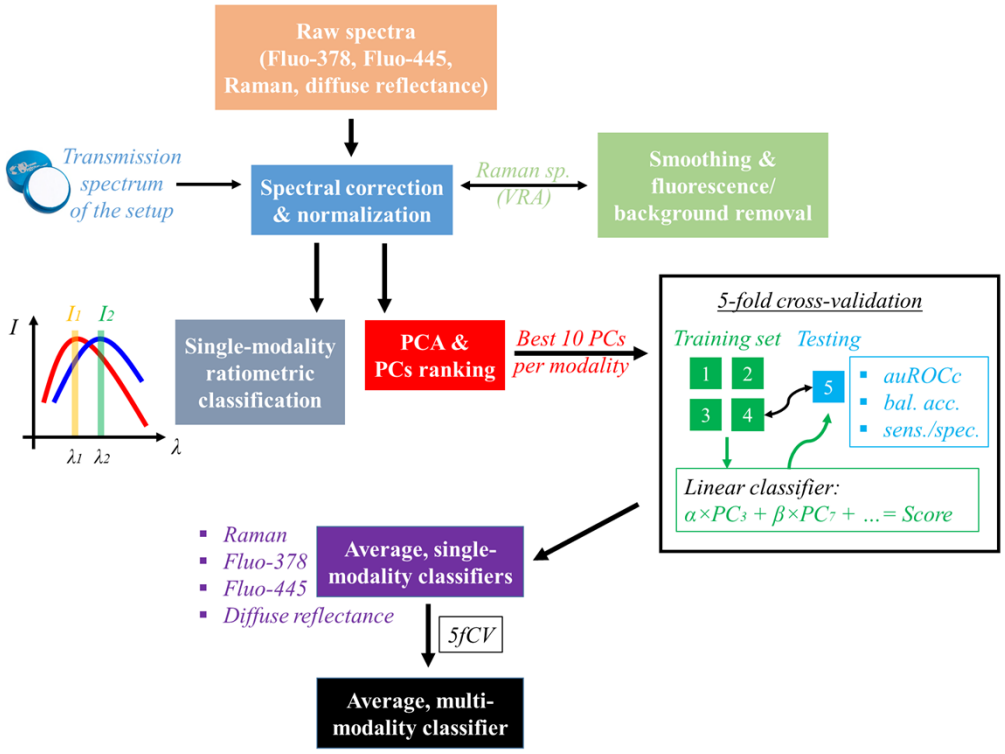


**Fig. 2.** Flowchart of the data analysis performed for the discrimination of two tissue types. Firstly, raw spectra from all techniques are corrected for the transmission spectrum of the setup and normalized in intensity; before normalization, Raman spectra are also processed through the Vancouver Raman Algorithm (VRA) routine. Secondly, the spectra are analyzed by two alternative methods based, respectively, on ratiometric scoring and PCA. For each spectral modality, the latter uses a linear combination of PCs for maximizing the separation between the two tissues; a 5-fold cross-validation routine selects the proper number of PCs and generates 5 classifiers, that can be averaged together. Finally, the average classifiers obtained from all 4 techniques can be linearly combined into a multimodal scoring algorithm through another cross-validation routine.

discarded the 13$^{th}$, 14$^{th}$ and 15$^{th}$ PCs from both diffuse reflectance and Fluo-445 datasets, due to their lack of relevant spectral information.

### 2.4.2. Spectral classification algorithms

The goal of this study is to discriminate three brain tissue types – tumor, dysplasia, and control – based on their Raman, diffuse reflectance and fluorescence spectral properties. To this end, we adopted two alternative classification methods.

The first method is based on ratiometric scoring, i.e. calculating the ratio between photon counts recorded at two different spectral bands (10-nm-wide for fluorescence and reflectance analysis, 30-cm$^{-1}$-wide for Raman) of each spectrum. Specifically, we can select the bands providing the best differentiation between each pairwise comparison (e.g. control vs dysplasia, control vs tumor, and dysplasia vs tumor); the bands used in this study are reported in the Results section. Hence, the ratiometric classifiers resulting from this approach can be used to differentiate Raman/fluorescence/reflectance spectra belonging to different tissue types. The Receiver Operating Characteristic (ROC) curve of each classifier and its area under the curve

Biomedical Optics EXPRESS

(auROCc) are then calculated, with the latter estimating the discriminatory power [23] of the corresponding spectral ratio. This method is simple and easily implementable, and can provide useful insights on tissue properties, although it exploits only a small part of the recorded spectral data.

The second method consists of building a binary classifier per spectral technique and per pair of tissue types, following a methodology similar to the one described in [16]. Each classifier is a linear combination of PCs that maximizes the auROCc between control and dysplastic / control and neoplastic / dysplastic and neoplastic spectra. Specifically, the PC loadings of each spectrum are multiplied by coefficients randomly generated through an automated, custom-made algorithm implemented in LabVIEW (National Instruments, Austin, Texas) and then summed together into a single score. The corresponding ROC curve and auROCc value are then calculated and recorded. The LabVIEW algorithm iterates such routine, each time comparing the new auROCc value with the maximum value among those ones already calculated, and stops after $N$ consecutive iterations (e.g., $N = 1000$) when convergence is reached, and no further maximum is found. Finally, the linear combination providing the best auROCc is saved, and the threshold corresponding to maximum balanced accuracy (i.e. the mean value between sensitivity and specificity values) can be used to classify a group of unknown spectra.

#### 2.4.3. Cross-validation and PCs selection

During the PCs-based analysis described above, each spectral dataset is organized between training and testing groups through a 5-fold cross-validation (5fCV) procedure. The data of each tissue class (control/dysplasia/tumor) are divided in 5 batches of similar sizes, and all the spectra recorded from the same patient are included in a single batch only; the same partition has been applied equally for all spectral techniques. For each round of the cross-validation, two batches (one from each tissue class) are used as testing group, while all remaining batches constitute the training group. Then, the balanced accuracy in classifying testing spectra is evaluated and recorded; the 5-rounds-average value of this parameter estimates the goodness of the classification method.

The 5fCV procedure can be used to avoid the risk of overfitting the training dataset by selecting a proper number of PCs for the analysis. The 5fCV-average accuracy is calculated by including an incremental number of PCs, sorted according to their discriminatory power (i.e. by their individual auROCc value). The maximum value indicates how many PCs must be included, while the remaining ones have to be discarded. No more than 10 PCs were included in each analysis.

Finally, the average classifier derived from the 5 rounds is used for classifying the whole dataset and evaluating its specificity, sensitivity and auROCc values. The spectra recorded from the same patient can be classified either individually (providing a single-point, or SP, classification) or averaged between them (patient-level, or PL, classification). SP classification estimates the accuracy in detecting diseased areas (e.g. for potential applications in guiding the surgical removal of brain tissues), while PL classification estimates the accuracy in diagnosing the disease itself on each patient.

#### 2.4.4. Multimodal scoring

Each spectral technique (Raman, diffuse reflectance, Fluo-378, Fluo-445) typically provides complementary information to the others. More in detail, Raman spectroscopy allows identifying proteins and lipids based on their vibrational fingerprints, diffuse reflectance spectroscopy investigates tissue intrinsic chromophores, e.g. water and hemoglobin, autofluorescence targets endogenous nucleotides involved in metabolism, such as NADH and FAD. Therefore, after obtaining 5fCV-average classifiers from individual techniques, we built a linear combination of them into a single, multimodal scoring algorithm. For this analysis, we used Raman, fluorescence and diffuse reflectance scores as inputs to the algorithm and cross-validation procedure described

Biomedical Optics EXPRESS

in previous paragraphs. To weight equally all 4 spectroscopies, the scores of each technique and pairwise comparison were normalized to their absolute maximum value before the multimodal analysis.

## 3. Results

### 3.1. Single-modality analyses

#### 3.1.1. Diffuse reflectance spectroscopy

Figure 3 and Table 2 report the results obtained from the analysis of diffuse reflectance spectra. All tissue spectra have been normalized to an isosbestic point of oxy- and deoxy-hemoglobin (570 nm) to take advantage of their different molar extinction coefficients and to qualitatively compare their relative abundance. Such an approach rests on the assumption that hemoglobin is the major absorber in the observed spectral region (450-710 nm). In fact, Fig. 3(A) shows the characteristic oxy-hemoglobin absorption peaks at 540 and 575 nm in all three tissues. Moreover, tumor and dysplasia are characterized by increased relative absorption with respect to control brain areas in both the 450-520 nm and in the 600-710 nm ranges, where the latter possibly suggests a higher concentration of deoxy-hemoglobin with respect to oxy-hemoglobin. Although retrieved from *ex vivo* tissues, these findings are consistent with previous results observed *in vivo* from an animal model [16], where brain tumors showed decreased levels of tissue oxygenation (hence, a lower oxy-to-deoxy hemoglobin content ratio), and from human pediatric patients [15], where neoplastic sites showed significantly lower diffuse reflectance intensities both below 520 nm and above 600 nm with respect to normal cerebral cortex. We tried exploiting the differences observed in the diffuse reflectance spectra through ratiometric classification, i.e. by measuring the intensity ratio between two, 10-nm-wide, spectral bands for each spectrum belonging to one tissue type or the other. Table 2 reports the bands used for each pairwise tissue comparison. The best discrimination between neoplastic/dysplastic and control spectra was obtained by using one band @540 nm and another one in the 515-520 nm region; such approach provided relatively high specificity (>90%), but low sensitivity (≤60%). On the other hand, the best separation between tumor and dysplasia was achieved @555 nm, which corresponds to a major deoxy-hemoglobin peak.

**Table 2. Summary from the analysis of diffuse reflectance spectra[a]**

| DIFFUSE REFLECT. | $I_1$ / $I_2$ (nm) | auROCc (%) | SP Spec. / Sens. (%) | Selected PCs | auROCc (%) | SP Spec. / Sens. (%) | PL Spec. / Sens. (%) |
|---|---|---|---|---|---|---|---|
| **CTRL vs TUM** | 551 / 519 | 76.0 | 90.7 / 53.3 | $PC_1$–$PC_4$, $PC_6$–$PC_8$, $PC_{10}$, $PC_{11}$ | 79.4 | 80.0 / 70.4 | 80 / 67 |
| **CTRL vs DYS** | 540 / 514 | 84.7 | 96.8 / 60.0 | $PC_1$, $PC_2$, $PC_5$, $PC_7$ | 89.8 | 73.3 / 92.6 | 60 / 92 |
| **DYS vs TUM** | 556 / 571 | 74.7 | 68.1 / 77.8 | $PC_2$–$PC_8$, $PC_{10}$, $PC_{11}$ | 80.0 | 87.2 / 66.7 | 80 / 62 |

[a]First four columns from the left: results obtained from ratiometric scoring, i.e. by measuring the intensity ratio between two, 10-nm-wide, spectral bands. Last four columns: results obtained from linearly combining the PCs selected through 5fCV procedure. For both classification methods, reported specificity and sensitivity values correspond to maximum balanced accuracy; results from the PC-based methodology are divided between single-point and patient-level classification.

A method based on linear combination of PC loadings slightly improved classification accuracies. Firstly, a 5fCV procedure determined the proper number of PCs to be included for each pairwise comparison. Secondly, the average classifier obtained from the 5 rounds of the cross-validation routine was used to derive ROC, auROCc, and the highest balanced accuracy

Biomedical Optics EXPRESS

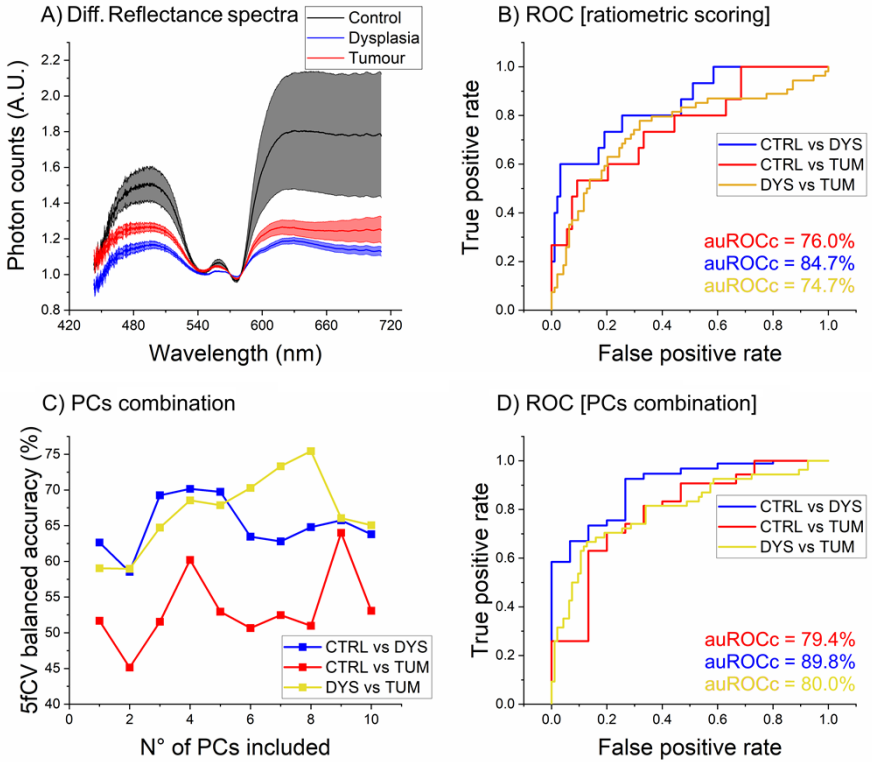


**Fig. 3.** A) Mean diffuse reflectance spectra ± standard errors (SEs) recorded from brain tumor, dysplasia and control tissue biopsies – red, blue and black lines, respectively. B) ROC curves obtained through ratiometric scoring: red line for "control vs tumor", blue for "control vs dysplasia", and magenta for "dysplasia vs tumor". Each auROCc is reported with the corresponding color. C) Average balanced accuracy of each pairwise comparison, obtained from a linear combination of PC loadings with 5fCV. This procedure was iterated by including an incremental number of PCs. D) Average ROC curves obtained from the 5fCV procedure and by selecting the best number of PC loadings.

value. This approach led to higher sensitivity towards tumor and dysplastic tissues (70.4% and 92.6%, respectively), but also reduced specificity to 80.0% and 73.3%. The major improvements were made in separating brain tumor from dysplasia, reaching 80.0% auROCc. More in general, discriminating dysplasia from control areas represents the best application for diffuse reflectance (89.8% auROCc); when classification scores are averaged into a single, "global" value for each patient (PL classification), 60% specificity and 92% sensitivity are achieved.

### 3.1.2. Fluorescence spectroscopy

Figure 4 and 5 show the results obtained from the analysis of fluorescence spectra excited, respectively, at 378 nm and 445 nm, while Tables 3 and 4 summarize classification accuracies obtained through both ratiometric scoring and PCs combination.

Fluorescence control spectra are characterized by a single peak around 516 / 523 nm for UV / blue excitation, respectively, while tumor spectra show a 3-nm redshift for both excitation wavelengths (Fig. 4(A) and 5(A)). An equal redshift can be observed for dysplasia, but only for 445-nm-excitation. These observations may reflect different relative concentrations in the main brain fluorophores: NADH [17,24] (with peak emission at 470 nm; excitable only with the 378 nm laser), FAD (530 nm) and collagen (450 / 490 nm for 378 / 445 nm laser light, since

Biomedical Optics EXPRESS

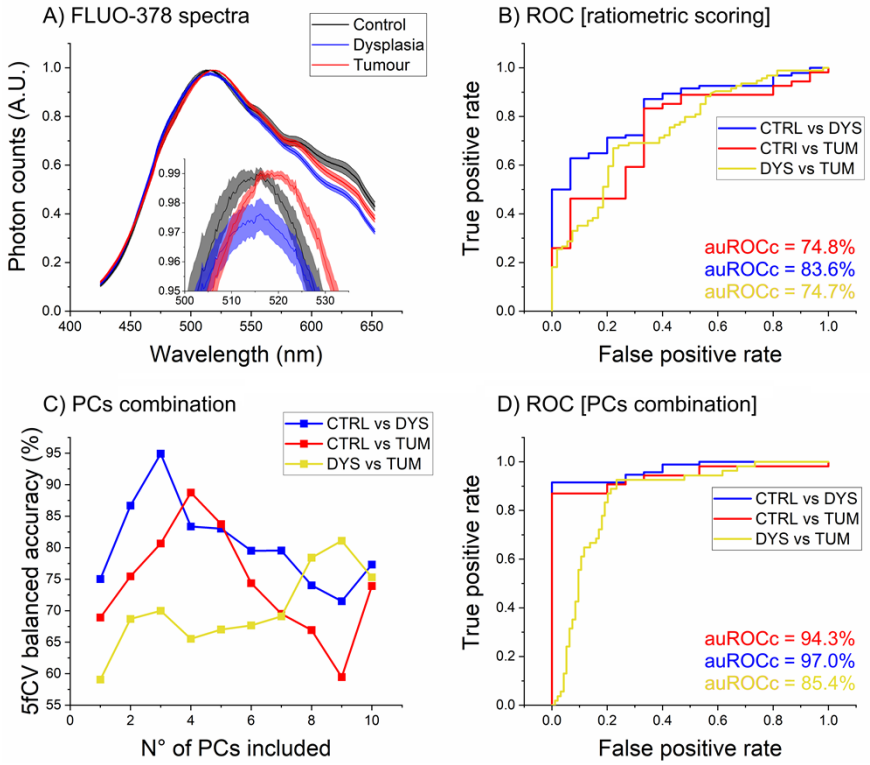


**Fig. 4.** A) Mean, UV-excited fluorescence spectra ± SEs recorded from brain tumor, dysplasia and control tissue biopsies – red, blue and black lines, respectively. An inset highlights the position of corresponding fluorescence emission peaks. B) ROC curves obtained through ratiometric scoring: red line for "control vs tumor", blue for "control vs dysplasia", and magenta for "dysplasia vs tumor". Each auROCc is reported with the corresponding color. C) Average balanced accuracy of each pairwise comparison, obtained from a linear combination of PC loadings with 5fCV. This procedure was iterated by including an incremental number of PCs. D) Average ROC curves obtained from the 5fCV procedure and by selecting the best number of PC loadings.

**Table 3. Summary from the analysis of fluorescence spectra excited at 378 nm[a]**

| FLUO-378 | $I_1$ / $I_2$ (nm) | auROCc (%) | SP Spec. / Sens. (%) | Selected PCs | auROCc (%) | SP Spec. / Sens. (%) | PL Spec. / Sens. (%) |
|---|---|---|---|---|---|---|---|
| **CTRL vs TUM** | 543 / 647 | 74.8 | 66.7 / 83.3 | $PC_2$, $PC_8$, $PC_{10}$, $PC_{11}$ | 94.3 | 100.0 / 87.0 | 100 / 86 |
| **CTRL vs DYS** | 583 / 647 | 83.6 | 93.3 / 62.8 | $PC_2$, $PC_8$, $PC_{11}$ | 97.0 | 100.0 / 91.5 | 100 / 92 |
| **DYS vs TUM** | 647 / 633 | 74.7 | 77.8 / 67.0 | $PC_1$, $PC_2$, $PC_5$–$PC_{10}$, $PC_{12}$ | 85.4 | 76.6 / 92.6 | 60 / 91 |

[a]First four columns from the left: results obtained from ratiometric scoring by using two, 10-nm-wide, spectral bands. Last four columns: results obtained from linearly combining the PCs selected through 5fCV procedure.

Biomedical Optics EXPRESS

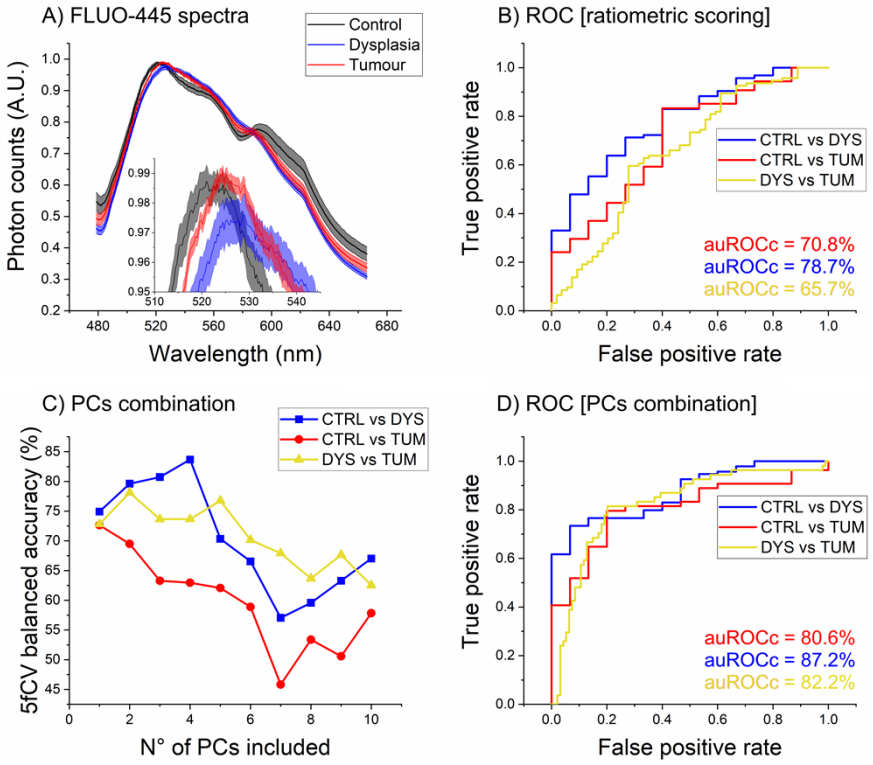


**Fig. 5.** A) Mean, blue-excited fluorescence spectra ± SEs recorded from brain tumor, dysplasia and control tissue biopsies – red, blue and black lines, respectively. An inset highlights the position of corresponding fluorescence emission peaks. B) ROC curves obtained through ratiometric scoring: red line for "control vs tumor", blue for "control vs dysplasia", and magenta for "dysplasia vs tumor". Each auROCc is reported with the corresponding color. C) Average balanced accuracy of each pairwise comparison, obtained from a linear combination of PC loadings with 5fCV. This procedure was iterated by including an incremental number of PCs. D) Average ROC curves obtained from the 5fCV procedure by selecting the best number of PC loadings.

**Table 4. Summary from the analysis of fluorescence spectra excited at 445 nm[a]**

| FLUO-445 | $I_1$ / $I_2$ (nm) | auROCc (%) | SP Spec. / Sens. (%) | Selected PCs | auROCc (%) | SP Spec. / Sens. (%) | PL Spec. / Sens. (%) |
|---|---|---|---|---|---|---|---|
| **CTRL vs TUM** | 589 / 644 | 70.8 | 60.0 / 83.3 | $PC_{10}$ | 80.6 | 80.0 / 79.6 | 80 / 76 |
| **CTRL vs DYS** | 577 / 657 | 78.7 | 80.0 / 63.8 | $PC_2$, $PC_4$, $PC_6$, $PC_{11}$ | 87.2 | 93.3 / 73.4 | 100 / 64 |
| **DYS vs TUM** | 659 / 641 | 65.7 | 72.2 / 59.6 | $PC_9$, $PC_{10}$ | 82.2 | 79.8 / 81.5 | 72 / 81 |

[a]First four columns from the left: results obtained from ratiometric scoring by using two, 10-nm-wide, spectral bands. Last four columns: results obtained from linearly combining the PCs selected through 5fCV procedure.

Biomedical Optics EXPRESS

its emission peak shifts together with excitation wavelength [25,26]). Hemoglobin, too, seems to play an important role in brain fluorescence spectra. As discussed, both in Nazeer et al. (2013 [27]) and Lin et al. (2001 [28]), higher/lower hemoglobin concentrations may cause the fluorescence emission maximum to shift. A modulation in the region between 540 and 580 nm is visible for both excitation wavelengths and corresponds to oxy-hemoglobin absorption peaks.

Finally, there are significant differences between the relative intensities recorded in the 600-650 nm region, following the same trend observed through diffuse reflectance spectroscopy: highest intensity in control tissues, lowest in dysplasia, and tumor spectra in between, possibly suggesting different deoxyhemoglobin contents. Other known fluorophores [24,27] are lipids (with broad emissions between 500 nm and 600 nm [29]) and porphyrins, although the latter should be recognizable by two characteristic peaks (630 nm and 700 nm) that are not clearly visible in our spectra.

All fluorescence-based ratiometric algorithms exploited the spectral differences observed at longer wavelengths by centering one 10-nm band at ~650 / ~660 nm for UV / blue excitation, respectively. Control tissues were discriminated by setting the other band on the hemoglobin peaks, while the best separation between tumor and dysplasia was determined by their respective slopes in the 630-660 nm region. In general, the two excitation wavelengths generated symmetric results (e.g. high sensitivity and low specificity in detecting tumor against control tissues, and vice versa for dysplasia), but UV-excitation provided better discrimination – although limited between ~75% and ~84% auROCc – in all pairwise comparisons. Another relevant feature was that, between the two diseases, dysplasia exhibits larger spectral differences when compared to control brain (as already observed from diffuse reflectance spectral data and analysis).

Significant improvements in tissue classification were achieved through PCs combination. UV-excited control spectra were successfully recognized with 100.0% specificity against both brain tumor and dysplasia, whose SP sensitivity reached 87.0% and 91.5%, respectively, and similarly to PL classification. Moreover, tumor SP sensitivity against dysplastic tissues increased from 67.0% to 92.6%, resulting in 85.4% auROCc. The classifiers for blue-excited spectra produced an almost equivalent outcome in discriminating tumor and dysplasia, but performed worse than UV-excitation in both healthy-vs-disease comparisons: specifically, providing lower specificity and sensitivity in tumor detection, and lower sensitivity in recognizing dysplastic areas.

#### 3.1.3. Raman spectroscopy

Figure 6 and Table 5 report the results obtained from the analysis of Raman spectra obtained after removing NIR fluorescence and background signals. These spectra are characterized by 5 main Raman bands in the fingerprint region (900-1800cm$^{-1}$) highlighted in Fig. 6(A): 940-960 cm$^{-1}$, 1030-1110 cm$^{-1}$, 1230-1350 cm$^{-1}$, 1420-1460 cm$^{-1}$, and 1610-1690 cm$^{-1}$, all of them typically generated by inelastic scattering from proteins and/or lipids [30–32]. In particular: Raman emissions from collagen contribute to the first four bands; the 3$^{rd}$ band can also be associated with amide III; the 4$^{th}$ band reflects the presence of lipids; the 5$^{th}$ band is associated with amide I; and, finally, nucleic acids can generate Raman signals within the 2$^{nd}$ and 3$^{rd}$ bands. All tissue spectra share similar relative intensities at 1300 cm$^{-1}$ and 1650 cm$^{-1}$. With respect to control specimens, however, both diseases show higher signal around 1060 cm$^{-1}$ and (to a lesser extent) 1650 cm$^{-1}$, while being characterized by lower signal at 950 cm$^{-1}$. Tumors are characterized by the highest and lowest intensities at, respectively, 1060 cm$^{-1}$ and 1440 cm$^{-1}$, while dysplasia exhibits the highest Raman emission in the 4$^{th}$ band. Consequently, the best ratiometric discrimination between control and tumor spectra was provided by the ratio between two, 30-cm$^{-1}$-wide bands near the 1440 cm$^{-1}$ and 1650 cm$^{-1}$ peaks, resulting in 93.3% SP specificity and 92.6% SP sensitivity. The 4$^{th}$ band was used also to separate tumor from dysplastic spectra (77.7%

Biomedical Optics EXPRESS

specificity, 66.7% sensitivity), while the 2nd and the 3rd served for the healthy-vs-dysplasia comparison (80.0% specificity, 76.6% sensitivity).

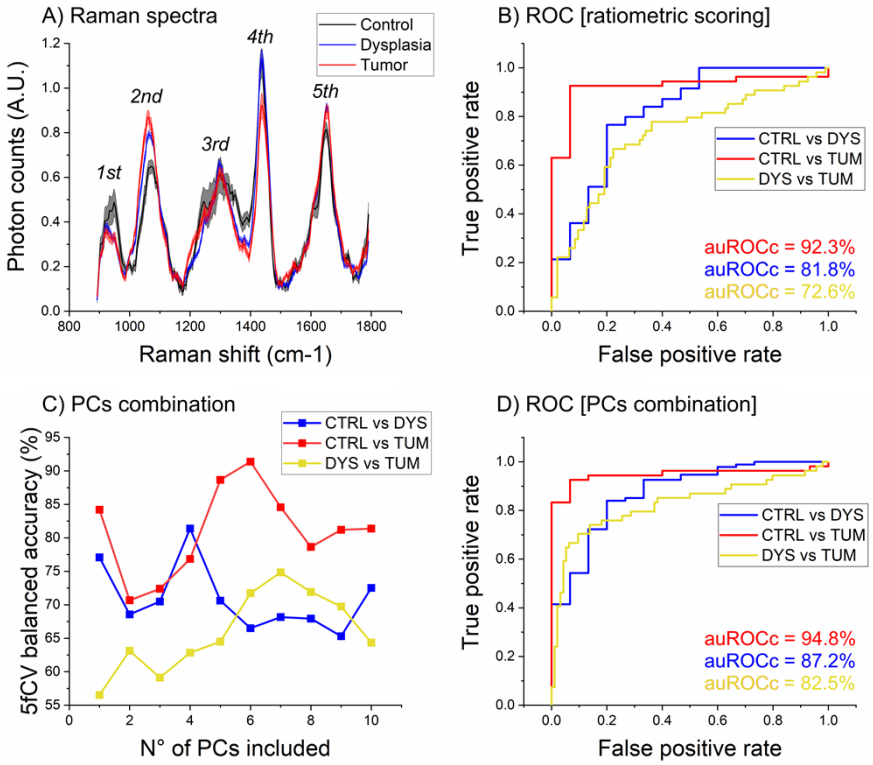


**Fig. 6.** A) Mean Raman spectra ± SEs recorded from brain tumor, dysplasia and control tissue biopsies – red, blue and black lines, respectively. The 5 major bands within the fingerprint region (600-1800cm$^{-1}$) are labelled. B) ROC curves obtained through ratiometric scoring: red line for "control vs tumor", blue for "control vs dysplasia", and magenta for "dysplasia vs tumor". Each auROCc is reported with the corresponding color. C) Average balanced accuracy of each pairwise comparison, obtained from a linear combination of PC loadings with 5fCV. This procedure was iterated by including an incremental number of PCs. D) Average ROC curves obtained from the 5fCV procedure by selecting the best number of PC loadings.

**Table 5. Summary from the analysis of Raman spectra excited at 785 nm[a]**

| RAMAN | $I_1$ / $I_2$ (cm$^{-1}$) | auROCc (%) | SP Spec. / Sens. (%) | Selected PCs | auROCc (%) | SP Spec. / Sens. (%) | PL Spec. / Sens. (%) |
|---|---|---|---|---|---|---|---|
| **CTRL vs TUM** | 1664 / 1398 | 92.3 | 93.3 / 92.6 | $PC_2$, $PC_3$, $PC_6$, $PC_8$, $PC_{12}$, $PC_{15}$ | 94.8 | 93.3 / 92.6 | 100 / 86 |
| **CTRL vs DYS** | 1012 / 1216 | 81.8 | 80.0 / 76.6 | $PC_2$, $PC_4$, $PC_8$, $PC_{11}$ | 87.2 | 80.0 / 84.0 | 80 / 80 |
| **DYS vs TUM** | 1216 / 1412 | 72.6 | 77.7 / 66.7 | $PC_1$–$PC_3$, $PC_{11}$–$PC_{14}$ | 82.5 | 90.4 / 70.4 | 84 / 76 |

[a]Change the table caption to: First four columns from the left: results obtained from ratiometric scoring by using two, 30-cm−1-wide, spectral bands. Last four columns: results obtained from linearly combining the PCs selected through 5fCV procedure.

Biomedical Optics EXPRESS

Classification based on PC loadings resulted in slightly higher auROCc values for the two control-vs-disease comparisons: 94.8% and 87.2% for tumor and dysplasia detection, respectively. This approach led to slightly higher SP sensitivity (84.0%) against dysplasia. On the other hand, differentiating tumors from dysplastic tissues received a significant improvement, reaching an average auROCc of 82.5% that is comparable to the results observed through the two fluorescence spectroscopies, while PL classification is slightly better (80% balanced accuracy vs ~76%).

### 3.2. Multimodal approach

The accuracies reported in Section 3.1 represent the ability of each spectroscopic technique in discriminating control, tumor and dysplastic brain tissues based on different biological features. Therefore, combining Raman, UV/blue-excited fluorescence and diffuse reflectance classifiers may provide a more comprehensive evaluation of the examined tissues.

For each pairwise comparison, the PCs-based scores previously obtained from all 4 techniques were linearly combined following the same procedure described in Sections 2.4.2 ad 2.4.3. A

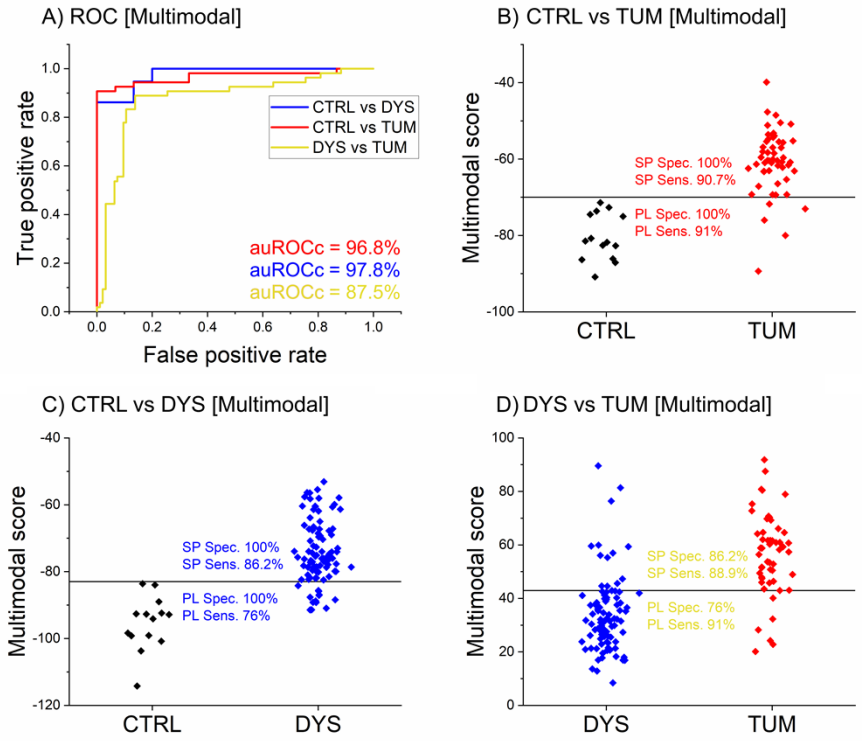


**Fig. 7.** A) Average ROC curves obtained from 5fCV procedures where Raman, fluorescence and diffuse reflectance scores were linearly combined into one multimodal classifier for each pairwise comparison; red line for "control vs tumor" comparison, blue for "control vs dysplasia", and magenta for "dysplasia vs tumor". Each auROCc is reported with the corresponding color. B) Multimodal scores obtained from the comparison between brain tumor (red points) and control (black points) tissue sites. C) Multimodal scores obtained from the comparison between brain dysplasia (blue points) and control (black points) tissue sites. D) Multimodal scores obtained from the comparison between brain tumor (red points) and dysplasia (blue points) tissue sites. The horizontal thresholds in B), C), D) correspond to the maximum balanced accuracies in discriminating tissues and to the reported SP and PL specificity and sensitivity values.

Biomedical Optics EXPRESS

5fCV-average classifier assigned multimodal scores to the corresponding tissue sites; then, we derived ROC curve and auROCc, SP/PL specificity and sensitivity values. The results are reported in Fig. 7. The multimodal approach allowed discriminating both pathological conditions from control tissue sites with 97÷98% auROCc, 100% specificity and high sensitivity for both SP (~91% and ~86% for brain tumors and dysplasia, respectively) and PL (91% and 76%) classification methods. Regarding dysplasia detection, the multimodal balanced accuracy was lower than the corresponding Fluo-378 value both in the SP (93.1% vs 95.8%) and especially in the PL (88% vs 96%) approaches. Such outcomes were due to the fact that the presented methodology a) favors auROCc maximization over accuracy maximization, and b) is optimized for SP classification. The multimodal approach was also successful in differentiating tumor and dysplastic tissues, achieving 87.5% auROCc and 85.7% SP balanced accuracy (84% PL).

Individual techniques already provided high classification accuracy for detecting either tumor (Raman being the best option) or dysplastic (UV-excited fluorescence being the best option) areas. Their combination further improved cancer recognition against control and dysplastic tissues, although resulting in no betterment for diagnosing dysplasia.

## 4. Discussion

The analysis of tumor and dysplastic brain biopsies collected from pediatric patients using multimodal fiber-probe spectroscopy allowed characterizing tissue optical properties and discriminating these two pathologies. Our analysis was conducted using both individual modalities and a multimodal approach in order to highlight advantages and drawbacks of each spectroscopic techniques as well as of their synergic use.

Regarding the individual use of spectroscopic techniques for diagnosing and classifying brain tumor tissue, few studies have been published using diffuse reflectance spectroscopy [14,15]. By examining various brain tissue types, including white matter, gray matter, and glioma, Gebhart and co-workers [14] found that the absorption spectra for the three tissue types are dominated by hemoglobin absorption in the spectral band below 600 nm. In fact, high levels of hemoglobin, possibly associated with tumor angiogenesis, and tissue hypoxia, which manifests itself with a decreased oxy-to-deoxy-hemoglobin ratio, are characteristics associated to tumor microenvironment [33] that has been discussed in previous studies based on *in vivo* application of diffuse reflectance spectroscopy [16,34]. In a more recent study performed *in vivo* on pediatric subjects [15], the authors found that diffuse reflectance spectral intensities between 600 nm and 800 nm are more effective in discriminating normal cortex from brain tumor than the spectral window below 600 nm. The associated diagnostic accuracy (auROCc) was 77%. Differently from previous studies carried out on adult brain tissues [14,35], the authors found cerebral cortex reflectance signals with higher intensity than the corresponding tumor signal over the whole examined spectral region. The authors stated that this discrepancy is probably due to the structural differences between adult and pediatric brain tumors. Hence, it is difficult to compare the results of our study obtained on pediatric subject with those obtained in adults. On the other hand, the diagnostic accuracy we obtained using diffuse reflectance signal (~79% auROCc) in discriminating control tissue against brain tumor agrees with the value of 77% obtained *in vivo* on pediatric subjects by Lin and co-workers [15]. Despite we obtained sensibly lower accuracy (~79% auROCc) in discriminating control and tumor tissues using diffuse reflectance than in a previous experiment on animal model (93% auROCc [16]) performed *in vivo* and with similar methodology, it is difficult to compare the data. In fact, the observed difference is due to both the structural difference between pediatric and rodent brain, and the physiological alterations occurring in the meantime between biopsy excision and spectral measurements. Anyway, being diffuse reflectance spectroscopy a technique sensible to tissue oxygenation, we can hypothesize that this technology would bring better results if implemented *in vivo*.

Biomedical Optics EXPRESS

On brain tissue diagnostic and classification, several studies employing tissue autofluorescence have been published in literature using slightly different approaches. To the best of our knowledge, the first study was performed by Lin and co-workers in 2000 [36], where the authors obtained 97% sensitivity and 96% specificity in discriminating normal against brain tumor tissues on *ex vivo* samples using 337 nm excitation. The same authors obtained 89% sensitivity and 76% specificity in a subsequent *in vivo* trial study [28] aimed at evaluating the applicability of optical spectroscopy for intrasurgical brain tumor demarcation. Saraswathy and co-workers [37] used a particular approach that employs multiple excitation wavelengths (from UV to blue spectral range) for detecting and staging brain tumors. By analyzing spectral data with PCA, they obtained 100% sensitivity and 100% specificity, but the statistical relevance of the study was limited, as the authors examined only 4/5 specimens. The use of a photosensitizer that causes the accumulation of fluorescent protoporphyrin IX within tumor tissue can improve the diagnostic accuracy to 93% sensitivity and 91% specificity, as demonstrated by Nazeer and co-workers [27]. Although the spectral emission of protoporphyrin IX is located in the red region of the spectrum, far apart from the autofluorescence peak, it is difficult to compare our results with the results obtained when a photosensitizer is used [27,38]. In our study, fluorescence excitation @378 nm seems better than @445 nm in differentiating all three tissue types, particularly tumors from control sites. In fact, we obtained 87% sensitivity and 100% specificity in discriminating brain tumor against control tissue when exciting @378 nm, 79,6% sensitivity and 80% specificity when exciting @445 nm. This suggests that NADH may play a role in both pathological conditions, as already known for brain tumors.

By using Raman spectroscopy, we observed lower lipids-to-proteins contribution in the spectra of brain tumors with respect to both control and dysplastic tissues, in agreement with what has been obtained in other *ex vivo* studies found in literature [39,40]. In the first study on pediatric brain tumors performed by Raman spectroscopy [41], Rabah and co-workers could distinguish between neuroblastoma and ganglioneuroma. In another study, the authors found a satisfying classification of pediatric neuroblastoma and other brain tumors using Raman spectroscopy [42]. Leslie and co-workers were able to discriminate glioma from normal brain tissue with an accuracy of 96.7% [43]. A similar level of accuracy, equal to 97%, was reached by Galli and co-workers [44] using near-infrared Raman spectroscopy in tandem with fluorescence spectroscopy on a statistically relevant number of patients. Zhou and co-workers employed both a ratiometric and a PCA-based method for classifying brain tumor against normal brain tissue using Raman spectroscopy [45]. In particular, in the discrimination of glioma against normal brain tissue, they obtained 100% sensitivity and 71.4% specificity using the ratiometric approach, whereas the sensitivity and specificity were 96.3% and 74.1% using the PCA-based analysis. In general, the 93.3% sensitivity and 92.6% specificity in discriminating brain tumor from control tissue obtained in our study are consistent with the values of sensitivity found in the above-mentioned literature and slightly higher in terms of diagnostic specificity. On the other hand, our sensitivity/specificity values are comparable to what has been obtained *in vivo* in two different studies performed by the same research group [11,46]. In a first study, performed using Raman spectroscopy alone, they obtained 93% sensitivity and 91% specificity in discriminating brain tumor from control tissue [46], whereas they reached 100% sensitivity and 93% specificity using combined Raman, diffuse reflectance, and fluorescence spectroscopy [11], demonstrating that a multimodal approach is advantageous for diagnosing brain tumor over individual spectroscopic techniques.

Regarding the classification of dysplastic tissue, the lack of sizable literature on the characterization of brain dysplasia through Raman, fluorescence or reflectance spectroscopies did not allow a meaningful comparison with our results. In dysplastic tissues, we observed slightly higher contributions in the nucleic acids/collagen/amide III Raman band (around 1300 $cm^{-1}$) and in the amide I band (around 1650 $cm^{-1}$) with respect to control sites, as found also in Anand et al. (2017 [18]).

Biomedical Optics EXPRESS

Although individual spectroscopic techniques – such as Raman and UV-excited fluorescence – provided high discriminatory power in differentiating control brain from neoplastic and dysplastic areas, our study shows that a multimodal approach can increase the accuracy in recognizing tumors against both control brain and dysplasia. Frequently, fluorescence and diffuse reflectance have been implemented in tandem within the same experimental setup [17,28,34,36]. In an *ex vivo* study, Lin and co-workers obtained 96% sensitivity and 93% specificity in discriminating gray matter from brain tumor by classifying the tissue with a ratiometric approach between fluorescence and diffuse reflectance data [36]. The same algorithm was employed by the same authors in a subsequent *in vivo* study [28] where they achieved 100% sensitivity and 76% specificity in discriminating tumor margins from normal brain tissue. In another study, brain tumor was delineated *in vivo* with 94% sensitivity and 94% specificity, using a photosensitizer in tandem with a combined fluorescence/reflectance optical probe [34]. The authors used fluorescence for analyzing both the endogenous fluorescence signal and those ones emitted by protoporphyrin IX and its photoproducts, whereas diffuse reflectance and light-transport modeling were used to extract hemoglobin concentration, tissue oxygenation and optical scattering parameters. High levels of hemoglobin – associated with tumor angiogenesis – also play a role by reabsorbing the excited fluorescence signal; this, in turn, contributes in shifting emission peaks and modulating fluorescence spectral profiles around oxy-hemoglobin absorption bands [28]. For this reason, the combined use of fluorescence and diffuse reflectance could help improving the diagnostic accuracy, as recently demonstrated by Lu and colleagues in an *ex vivo* study, where they obtained 89.3% sensitivity and 92.5% specificity in differentiating gray matter from brain tumor on specimens obtained from five patients. By combining Raman and fluorescence spectroscopies, Jermyn et al. (2017 [11]) achieved 98% auROCc and Anand et al. (2017 [18]) 96% auROCc for, respectively, tumor and dysplasia detection; the multimodal approach presented in this study obtained ≥97% in both tasks. On the other hand, to our knowledge no previous study attempted to discriminate between neoplastic and dysplastic tissues. Notably, even though the pathologies addressed in this work can coexist, their comparison has never been tested before through optical spectroscopy. In this regard, the combination of Raman, fluorescence and diffuse reflectance spectroscopies resulted in 87.5% auROCc and thus proved to be a capable diagnostic tool.

In brain surgery, avoiding false positives while identifying all areas to be resected is imperative. Our data, which subserve this purpose, constitute additional evidence in favor of translating optical spectroscopy to the clinical practice. In fact, multimodal spectroscopy could provide significant advantages for the intraoperative, label-free diagnosis of brain tissues with respect to current state-of-the-art methods. First of all, the information can be derived from both excised tissue biopsies and *in vivo* without the need of a biopsy or tissue processing and labelling. Then, the diagnostic information can be provided in a shorter amount of time with respect to the gold standard for tissue diagnostics, which is represented by histopathological examination. Spectroscopic data, although not provided in real-time since Raman or multimodal spectroscopy requires typically few seconds of integration time, are acquired and processed within tens of seconds rather than within tens of minutes, as for the intrasurgical histopathology, providing a significant advantage in terms of speed of the diagnostic workflow. Regarding the spatial resolution achievable in determining tumor margins, this is not subcellular as for the histopathological examination but it's high enough for guiding resection. In fact, the spatial resolution is determined by the sampling volume, which is in the hundreds of micron range. This value is comparable to the resolution achievable by using a bisturi during resection. Hence, the apparently low resolution of the multimodal spectroscopy approach won't have a significant impact in the precision of the resection. Moreover, the experimental setup implemented in this study is compact and transportable, hence it offers the potential to be used directly on living brain tissues, potentially guiding tissue resection with almost real-time feedback. Such developments could represent an important step in improving the clinical treatment of neoplastic and dysplastic

Biomedical Optics EXPRESS

brain diseases, with relevant consequences on healthcare efficiency and patients' well-being. The recent *in vivo* implementation of both Raman spectroscopy [46] and multimodal spectroscopy [11] for diagnosing and classifying brain tumor provides further support to the possibility of translating the technology from research labs to a surgical scenario.

## 5. Conclusions

In conclusion, multimodal fiber-probe spectroscopy allowed discriminating dysplastic and neoplastic brain tissue against control tissue with high values of sensitivity and specificity, paving the way for a potential clinical translation of the proposed approach. In particular, brain tumor/dysplasia were classified against control tissue with 91%/86% sensitivity and 100%/100% specificity, respectively. Brain tumor was discriminated from brain dysplasia using optical spectroscopy for the first time, reaching 89% sensitivity and 86% specificity. The multimodal spectroscopic approach was proved to be advantageous for diagnostic purposes over the individual spectroscopic techniques. In the near future, our plan is to better evaluate the translation potentiality of the technology by designing and developing an experimental setup useful for surgeons or to integrate the multimodal spectroscopic modality within existing optical instrumentation commonly found within the surgical scenario. Despite the promising results obtained in our study, much work has still to be done before translating multimodal optical spectroscopy from the optical research lab to the surgical bed.

**Funding.** Fondazione Cassa di Risparmio di Firenze (banking foundation; "Human Brain Optical Mapping"); Tuscany Region (projects DECODEE, GLIOMICS, research program PAR FAS 2007-2013); EU Horizon 2020 Research and Innovation Programme (grant 654148 Laserlab-Europe, grant 871277 AMPLITUDE); Italian Ministry for Education, University and Research (Flagship Project NANOMAX).

**Disclosures.** The authors declare no conflicts of interest.

**Data availability.** Data underlying the results presented in this paper are not publicly available at this time, but may be obtained from the authors upon reasonable request.

## References

1. J. Kabat and P. Król, "Focal cortical dysplasia – review," Pol. Przegl. Radiol. Med. Nukl. **77**(2), 35–43 (2012).
2. "Focusing on brain tumours and brain metastasis: editorial," *Nat. Rev. Cancer* 20, 1 (2020).
3. A. Nabavi, P. M. Black, D. T. Gering, C. F. Westin, V. Mehta, R. S. Pergolizzi Jr, M. Ferrant, S. K. Warfield, N. Hata, R. B. Schwartz, 3rd W. M. Wells, R. Kikinis, and F. A. Jolesz, "Serial intraoperative magnetic resonance imaging of brain shift," Neurosurgery **48**(4), 787–798 (2001).
4. T. Garzon-Muvdi, C. Kut, X. Li, and K. L. Chaichana, "Intraoperative imaging techniques for glioma surgery," Future Oncol. **13**(19), 1731–1745 (2017).
5. S. Anand, R. Cicchi, and F. S. Pavone, "Optical fiber-probe spectroscopy of brain tumors," in R. R. Alfano and L. Shi, *Nanophotonics, Neurophotonics and Biomedical Spectroscopy* (Elsevier, 2019), pp. 1–23.
6. F. Yamaguchi, "The border zone of tumor. where is the border? what is a surgical border for patients?" World Neurosurgery: X **2**, 100011 (2019).
7. Z. Ganji, M. Aghaee Hakak, S. A. Zamanpour, and H. Zare, "Automatic detection of focal cortical dysplasia type ii in mri: is the application of surface-based morphometry and machine learning promising?" Front. Hum. Neurosci. **15**, 608285 (2021).
8. M. Giulioni, G. Marucci, M. Martinoni, A. F. Marliani, F. Toni, F. Bartiromo, L. Volpi, P. Riguzzi, F. Bisulli, I. Naldi, R. Michelucci, A. Baruzzi, P. Tinuper, and G. Rubboli, "Epilepsy associated tumors: Review article," World J. Clin. Cases **2**(11), 623–641 (2014).
9. Y. Guo, Y. Liu, W. Ming, Z. Wang, J. Zhu, Y. Chen, L. Yao, M. Ding, and C. Shen, "Distinguishing focal cortical dysplasia from glioneuronal tumors in patients with epilepsy by machine learning," Front. Neurol. **11**, 548305 (2020).
10. P. Charalampaki, P. J. Proskynitopoulos, A. Heimann, and M. Nakamura, "5-aminolevulinic acid multispectral imaging for the fluorescence-guided resection of brain tumors: a prospective observational study," Front. Oncol. **10**, 1069 (2020).
11. M. Jermyn, J. Mercier, K. Aubertin, J. Desroches, K. Urmey, J. Karamchandiani, E. Marple, M.-C. Guiot, F. Leblond, and K. Petrecca, "Highly accurate detection of cancer in situ with intraoperative, label-free, multimodal optical spectroscopy," Cancer Res. **77**(14), 3942–3950 (2017).
12. J. Zhang, Y. Fan, M. He, X. Ma, Y. Song, M. Liu, and J. Xu, "Accuracy of Raman spectroscopy in differentiating brain tumor from normal brain tissue," Oncotarget **8**(22), 36824–36831 (2017).

Biomedical Optics EXPRESS


13. J. Desroches, M. Jermyn, M. Pinto, F. Picot, M.-A. Tremblay, S. Obaid, E. Marple, K. Urmey, D. Trudel, G. Soulez, M.-C. Guiot, B. C. Wilson, K. Petrecca, and F. Leblond, "A new method using Raman spectroscopy for in vivo targeted brain cancer tissue biopsy," Sci. Rep. **8**(1), 1792 (2018).
14. S. C. Gebhart, W.-C. Lin, and A. Mahadevan-Jansen, "*In vitro* determination of normal and neoplastic human brain tissue optical properties using inverse adding-doubling," Phys. Med. Biol. **51**(8), 2011–2027 (2006).
15. W.-C. Lin, D. I. Sandberg, S. Bhatia, M. Johnson, S. Oh, and J. Ragheb, "Diffuse reflectance spectroscopy for *in vivo* pediatric brain tumor detection," J. Biomed. Opt. **15**(6), 061709 (2010).
16. E. Baria, E. Pracucci, V. Pillai, F. S. Pavone, G. M. Ratto, and R. Cicchi, "In vivo detection of murine glioblastoma through Raman and reflectance fiber-probe spectroscopies," Neurophoton. **7**(04), 045010 (2020).
17. H. Lu, K. Grygoryev, N. Bermingham, M. Jansen, M. O'Sullivan, G. Nunan, K. Buckley, K. Manley, R. Burke, and S. Andersson-Engels, "Combined autofluorescence and diffuse reflectance for brain tumour surgical guidance: initial ex vivo study results," Biomed. Opt. Express **12**(4), 2432–2446 (2021).
18. S. Anand, R. Cicchi, F. Giordano, V. Conti, A. M. Buccoliero, R. Guerrini, and F. S. Pavone, "Multimodal fiber-probe spectroscopy allows detecting epileptogenic focal cortical dysplasia in children," J. Biophotonics **10**(6-7), 896–904 (2017).
19. E. Baria, R. Cicchi, F. Malentacchi, I. Mancini, P. Pinzani, M. Pazzagli, and F. S. Pavone, "Supervised learning methods for the recognition of melanoma cell lines through the analysis of their Raman spectra," J. Biophotonics **14**(3), 202000365 (2021).
20. R. Gunaratne, I. Monteath, J. Goncalves, R. Sheh, C. N. Ironside, M. Kapfer, R. Chipper, B. Robertson, R. Khan, and D. Fick, "Machine learning classification of human joint tissue from diffuse reflectance spectroscopy data," Biomed. Opt. Express **10**(8), 3889–3898 (2019).
21. E. Baria, S. Morselli, S. Anand, R. Fantechi, G. Nesi, M. Gacci, M. Carini, S. Serni, R. Cicchi, and F. S. Pavone, "Label-free grading and staging of urothelial carcinoma through multimodal fibre-probe spectroscopy," J. Biophotonics **12**(11), e201900087 (2019).
22. J. Zhao, H. Lui, D. I. McLean, and H. Zeng, "Automated autofluorescence background subtraction algorithm for biomedical Raman spectroscopy," Appl. Spectrosc. **61**(11), 1225–1232 (2007).
23. F. Li and H. He, "Assessing the accuracy of diagnostic tests," Shanghai Arch. Psychiatry **30**(3), 207–212 (2018).
24. F. Poulon, J. Pallud, P. Varlet, M. Zanello, F. Chretien, E. Dezamis, G. Abi-Lahoud, F. Nataf, B. Turak, B. Devaux, and D. Abi Haidar, "Real-time brain tumor imaging with endogenous fluorophores: a diagnosis proof-of-concept study on fresh human samples," Sci. Rep. **8**(1), 14888 (2018).
25. H. B. Manning, M. B. Nickdel, K. Yamamoto, J. L. Lagarto, D. J. Kelly, C. B. Talbot, G. Kennedy, J. Dudhia, J. Lever, C. Dunsby, P. French, and Y. Itoh, "Detection of cartilage matrix degradation by autofluorescence lifetime," Matrix Biol. **32**(1), 32–38 (2013).
26. J. R. Lakowicz, *Principles of Fluorescence Spectroscopy*, Third edition (Springer 2006), p. 65.
27. S. S. Nazeer, A. Saraswathy, A. K. Gupta, and R. S. Jayasree, "Fluorescence spectroscopy as a highly potential single-entity tool to identify chromophores and fluorophores: study on neoplastic human brain lesions," J. Biomed. Opt **18**(6), 067002 (2013).
28. W.-C. Lin, S. A. Toms, M. Johnson, E. D. Jansen, and A. Mahadevan-Jansen, "In vivo brain tumor demarcation using optical spectroscopy," Photochem. Photobiol. **73**(4), 396–402 (2001).
29. G. A. Wagnières, W. M. Star, and B. C. Wilson, "In vivo fluorescence spectroscopy and imaging for oncological applications," Photochem. Photobiol. **68**(5), 603–632 (1998).
30. B. Brozek-Pluska, K. Miazek, J. Musiał, and R. Kordek, "Label-free diagnostics and cancer surgery Raman spectra guidance for the human colon at different excitation wavelengths," RSC Adv. **9**(69), 40445–40454 (2019).
31. S. Feng, S. Huang, D. Lin, G. Chen, Y. Xu, Y. Li, Z. Huang, J. Pan, R. Chen, and H. Zeng, "Surface-enhanced Raman spectroscopy of saliva proteins for the noninvasive differentiation of benign and malignant breast tumors," Int. J. Nanomed. **10**, 537–547 (2015).
32. M. Pinto, K. C. Zorn, J.-P. Tremblay, J. Desroches, F. Dallaire, K. Aubertin, E. Marple, C. Kent, F. Leblond, D. Trudel, and F. Lesage, "Integration of a Raman spectroscopy system to a robotic-assisted surgical system for real-time tissue characterization during radical prostatectomy procedures," J. Biomed. Opt. **24**(02), 1 (2019).
33. B. Muz, P. de la Puente, F. Azab, and A. K. Azab, "The role of hypoxia in cancer progression, angiogenesis, metastasis, and resistance to therapy," Hypoxia (Auckl) **3**, 83–92 (2015).
34. P. A. Valdés, A. Kim, F. Leblond, O. M. Conde, B. T. Harris, K. D. Paulsen, B. C. Wilson, and D. W. Roberts, "Combined fluorescence and reflectance spectroscopy for in vivo quantification of cancer biomarkers in low- and high-grade glioma surgery," J. Biomed. Opt. **16**(11), 116007 (2011).
35. H. R. Eggert and V. Blazek, "Optical properties of human brain tissue, meninges, and brain tumors in the spectral range of 200 to 900 nm," Neurosurgery **21**(4), 459–464 (1987).
36. W.-C. Lin, S. A. Toms, M. Motamedi, E. D. Jansen, and A. Mahadevan-Jansen, "Brain tumor demarcation using optical spectroscopy; an in vitro study," J. Biomed. Opt **5**(2), 214–220 (2000).
37. A. Saraswathy, R. S. Jayasree, K. V. Baiju, A. K. Gupta, and V. P. Mahadevan Pillai, "Optimum wavelength for the differentiation of brain tumor tissue using autofluorescence spectroscopy," Photomed. Laser Surg. **27**(3), 425–433 (2009).
38. H. Xie, N. Haj-Hosseini, J. Richter, K. Wardell, and S. Andersson-Engels, "Fluorescence spectroscopy for guiding malignant brain tumor resection with optical touch pointer," Asia Commun. Photonics Conf. Exhib. (2010), 46–47.

Biomedical Optics EXPRESS


39. C. Krafft, S. B. Sobottka, G. Schackert, and R. Salzer, "Near infrared Raman spectroscopic mapping of native brain tissue and intracranial tumors," Analyst **130**(7), 1070–1077 (2005).
40. S. Koljenović, T. C. Bakker Schut, R. Wolthuis, B. de Jong, L. Santos, P. J. Caspers, J. M. Kros, and G. J. Puppels, "Tissue characterization using high wave number Raman spectroscopy," J. Biomed. Opt. **10**(3), 031116 (2005).
41. R. Rabah, R. Weber, G. K. Serhatkulu, A. Cao, H. Dai, A. Pandya, R. Naik, G. Auner, J. Poulik, and M. Klein, "Diagnosis of neuroblastoma and ganglioneuroma using Raman spectroscopy," J. Pediatr. Surg. **43**(1), 171–176 (2008).
42. H. Wills, R. Kast, C. Stewart, R. Rabah, A. Pandya, J. Poulik, G. Auner, and M. D. Klein, "Raman spectroscopy detects and distinguishes neuroblastoma and related tissues in fresh and (banked) frozen specimens," J. Pediatr. Surg. **44**(2), 386–391 (2009).
43. D. G. Leslie, R. E. Kast, J. M. Poulik, R. Rabah, S. Sood, G. W. Auner, and M. D. Klein, "Identification of pediatric brain neoplasms using Raman spectroscopy," Pediatr. Neurosurg. **48**(2), 109–117 (2012).
44. R. Galli, M. Meinhardt, E. Koch, G. Schackert, G. Steiner, M. Kirsch, and O. Uckermann, "Rapid label-free analysis of brain tumor biopsies by near infrared raman and fluorescence spectroscopy—a study of 209 patients," Front. Oncol. **9**, 1165 (2019).
45. Y. Zhou, C.-H. Liu, B. Wu, X. Yu, G. Cheng, K. Zhu, K. Wang, C. Zhang, M. Zhao, R. Zong, L. Zhang, L. Shi, and R. R. Alfano, "Optical biopsy identification and grading of gliomas using label-free visible resonance Raman spectroscopy," J. Biomed. Opt. **24**(09), 1–12 (2019).
46. M. Jermyn, K. Mok, J. Mercier, J. Desroches, J. Pichette, K. Saint-Arnaud, L. Bernstein, M.-C. Guiot, K. Petrecca, and F. Leblond, "Intraoperative brain cancer detection with Raman spectroscopy in humans," Sci. Transl. Med. **7**(274), 274ra19 (2015).